

Aerothermodynamic Characteristics of Flat-Nose Power-Law Bodies in Low-Density Hypersonic Flow

Wilson F. N. Santos*

*National Institute for Space Research
Cachoeira Paulista, SP 12630-000 BRAZIL*

The steady-state aerodynamic characteristics of a new family of blunted leading edges immersed in high-speed rarefied air flow are examined by using a Direct Simulation Monte Carlo Method. A very detailed description of the aerodynamic surface quantities on the bodies has been presented by a numerical method that properly accounts for non-equilibrium effects that arise near the nose of the leading edges and that are especially important at high Mach number. Comparisons based on geometry are made between these blunt configurations and circular cylinder shapes. Some significant differences between these shapes is noted on the aerodynamic surface quantities. It is found that the heat transfer coefficient at the stagnation point decreased with increasing the flat-nose of the leading edges. The analysis also showed that, despite the seeming advantages of the new blunt shapes, circular cylinder still provides smaller stagnation point heating, however large total drag under the range of condition investigated.

Nomenclature

a	Constant in power-law body equation, Eq.(1)
C_d	Drag coefficient, $2D/\rho_\infty V_\infty^2 H$
C_f	Skin friction coefficient, $2\tau_w/\rho_\infty V_\infty^2$
C_h	Heat transfer coefficient, $2q_w/\rho_\infty V_\infty^3$
C_p	Pressure coefficient, $2(p_w - p_\infty)/\rho_\infty V_\infty^2$
D	Drag force, N
d	Molecular diameter, m
H	Body height at the base, m
Kn	Knudsen number, λ/l
L	Body length, m
l	Characteristic length, m
M	Mach number
m	Molecular mass, kg
N	Number flux, $m^{-2}s^{-1}$
n	Body power law exponent
p	Pressure, N/m^2
q	Heat flux, W/m^2
R	Circular cylinder radius, m
Re	Reynolds number, $\rho V l/\mu$
s	Arc length, m

*Researcher, Combustion and Propulsion Laboratory. AIAA Member.

T	Temperature, K
t	Leading edge thickness, m
V	Velocity, m/s
X	Mole fraction
x, y	Cartesian axes in physical space, m
y_{nose}	Half thickness of the leading edge, m
η	Coordinate normal to body surface, m
θ	Wedge half angle, deg
λ	Mean free path, m
ξ	Coordinate tangent to body surface, m
ρ	Density, kg/m ³
τ	Shear stress, N/m ²
ω	Viscosity index

Subscript

cyl	Circular cylinder
o	Stagnation point conditions
pw	Power law
w	Wall conditions
∞	Freestream conditions

I. Introduction

ONE of the key issues concerning hypersonic configurations is the leading edge of the vehicle. Hypersonic configurations are generally characterized by slender bodies and sharp leading edges in order to achieve good aerodynamic properties like high lift and low drag. Nevertheless, for flight at hypersonic speeds, the vehicle leading edges must be sufficiently blunt in order to reduce the heat transfer rate to acceptable levels, and possibly to allow for internal heat conduction. The use of blunt-nose shapes tends to alleviate the aerodynamic heating problem since the heat flux for blunt bodies is far lower than that for sharply pointed bodies. In addition, the reduction in heating rate for a blunt body is accompanied by an increase in heat capacity, due to the increased volume. Therefore, designing a hypersonic vehicle leading edge involves a tradeoff between making the leading edge sharp enough to obtain acceptable aerodynamic and propulsion efficiency and blunt enough to reduce the aerodynamic heating in the stagnation point. In this context, power law shaped leading edges ($y \propto x^n, 0 < n < 1$) have been considered as especially promising bluntness for hypersonic configurations in order to provide the leading edge heating and manufacturing requirements. This concept is based on the work of Mason and Lee¹, who have pointed out that, for certain exponents, power law shapes exhibit both blunt (infinite body slope at the nose) and sharp (zero radius of curvature at the nose) characteristics. They suggested the possibility of a difference between shapes that are geometrically sharp and shapes that behave aerodynamically as if they were sharp. Their analysis describes the details of the geometry and aerodynamics of low-drag axisymmetric bodies by using Newtonian theory. However, one of the important aspects of the problem, stagnation point heat transfer, was not considered.

A great deal of works²⁻⁹ has been carried out recently on power-law form representing blunt geometries. The major interest in these works has gone into considering the power-law shape as possible candidates for blunting geometries of hypersonic leading edges, such as hypersonic waverider vehicles¹⁰ which have been lately considered for high-altitude/low-density applications¹¹⁻¹⁴.

Through the use of Direct Simulation Monte Carlo (DSMC) method, Santos and Lewis⁴ have investigated the sensitivity of the stagnation point heating and total drag to shape variations of such leading edges for the idealized situation of two-dimensional rarefied hypersonic flow at zero angle of incidence. The emphasis of the work was to compare power law leading edges with round leading edges (circular cylinder) in order to determine which geometry would be better suited as a blunting profile in terms of stagnation point heating

and total drag coefficient. Their analysis showed that power law leading edges provided smaller total drag and larger stagnation point heating than the corresponding circular cylinder that generated the power law shapes under the range of conditions investigated.

II. Motivation

In the present work a new investigation of a stagnation point heating reduction concept for hypersonic flow on power law shapes is conducted. According to Reller¹⁵, a method of designing low heat transfer bodies is devised on the premise that the rate of heat transfer to the nose will be low if the local velocity is low, while the rate of heat transfer to the afterbody will be low if the local density is low. A typical body that results from this design method consists of a flat nose followed by a highly curved, but for the most part slightly inclined, afterbody surface. In this scenario, the purpose of this work is to examine computationally the aerodynamic surface quantities for a family of new contours, flat-nose power-law shapes, that satisfy these geometric constraints and to compare them to round leading edges in order to provide information on how well these shapes stand up as possible candidates for blunting geometries of hypersonic leading edges. The focus of the present study is the low-density region in the upper atmosphere. At high altitudes, and therefore low density, the molecular collision rate is low and the energy exchange occurs under non-equilibrium conditions. In such a circumstance, the conventional continuum gas dynamics that are based on the concept of local equilibrium is inappropriate, and an approach based on molecular gas dynamics is required for the analysis. Therefore, a DSMC method will be employed to calculate the rarefied hypersonic two-dimensional flow on the flat-nose leading edge shapes.

III. Leading Edge Geometry Definition

In dimensional form, the power law contours that define the shapes of the afterbody surfaces are given by the following expression,

$$y = y_{nose} + ax^n \quad (1)$$

where y_{nose} is the half thickness of the flat nose of the leading edges, n is the power law exponent and a is the power law constant which is a function of n .

The flat-nose power-law shapes are modeled by assuming a sharp leading edge (wedge) of half angle θ with a circular cylinder of radius R inscribed tangent to this wedge. The flat-nose power law shapes, inscribed between the wedge and the cylinder, are also tangent to both shapes at the same common point where they have the same slope angle. It was assumed a leading edge half angle of 10 degree, a circular cylinder diameter of 10^{-2} m, power law exponents of 2/3, 0.7, 3/4, and 0.8, and front surface thicknesses t/λ_∞ of 0, 0.01, 0.1 and 1, where $t = 2y_{nose}$ and λ_∞ is the freestream molecular mean free path. Figure 1 shows schematically this construction.

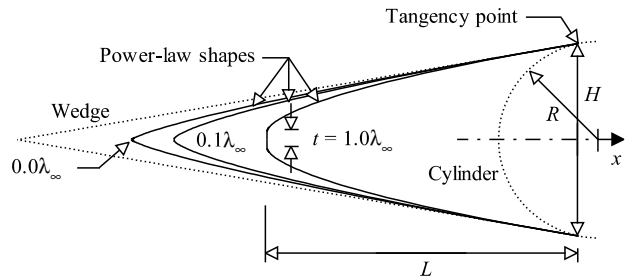


Figure 1. Drawing illustrating the leading edge geometries.

From geometric considerations, the power law constant a is obtained by matching slopes for the wedge, circular cylinder and power law body at the tangency point. The common body height H at the tangency point is equal to $2R \cos \theta$, and the body length L from the nose to the tangency point in the axis of symmetry is given by $n(H - t)/2 \tan \theta$. Since the wake region behind the power law bodies is not of interest in this investigation, it was assumed that the power law bodies are infinitely long but only the length L is considered.

IV. Methodology

The various phenomena found in high-speed flow are often described in terms of dimensionless parameters of the flow such as Reynolds number and Mach number. The former parameter may be considered to be a measure of the effect of viscosity and the latter parameter a measure of the effect of compressibility on the flowfield. An additional parameter, the Knudsen number, becomes important when considering rarefied flow. The Knudsen number, $Kn = \lambda/l$, is defined as the ratio of the mean free path λ of the molecules to a characteristic body dimension l . Traditionally, flows are divided into four regimes¹⁶: $Kn < 0.01$, continuum flow, $0.01 < Kn < 0.1$, slip flow, $0.1 < Kn < 10$, transitional flow, and $Kn > 10$, free molecular flow.

Flow in the regime of intermediate Knudsen numbers, $0.01 < Kn < 10$, is difficult to deal with analytically and, at this time, it appears that the Direct Simulation Monte Carlo (DSMC) method introduced by Bird¹⁷ is the most accurate and credible procedure for computing leading edge flows and surface effects in this flow regime. The DSMC method models the flow as being a large number of statistically representative particles, each one with a position, velocity and internal energy. The state of the particles is stored and modified with time as the particles move, collide, and undergo boundary interactions in simulated physical space.

The molecular collisions are modeled by using the variable hard sphere (VHS) molecular model¹⁸ and the no time counter (NTC) collision sampling technique¹⁹. The VHS model employs the simple hard sphere angular scattering law so that all directions are equally possible for post-collision velocity in the center-of-mass frame of reference. However, the collision cross section depends on the relative speed of colliding molecules. The intermolecular collisions are uncoupled to the translational molecular motion over the time step used to advance the simulation. Time is advanced in discrete steps such that each step is small in comparison with the mean collision time^{20,21}. The simulation is always calculated as unsteady flow. However, a steady flow solution is obtained as the large time state of the simulation.

The energy exchange between kinetic and internal modes is controlled by the Borgnakke-Larsen statistical model²². The essential feature of this model is that a part of collisions is treated as completely inelastic, and the remainder of the molecular collisions is regarded as elastic. Simulations are performed using a non-reacting gas model consisting of two chemical species, N_2 and O_2 . Energy exchanges between the translational and internal modes are considered. The probability of an inelastic collision determines the rate at which energy is transferred between the translational and internal modes after an inelastic collision. For a given collision, the probabilities are designated by the inverse of the relaxation numbers, which correspond to the number of collisions necessary, on average, for a molecule to relax. The relaxation numbers are traditionally given as constants, 5 for rotation and 50 for vibration.

In order to implement the particle-particle collisions, the flowfield is divided into an arbitrary number of regions, which are subdivided into computational cells. The cells are further subdivided into 4 subcells, 2 subcells/cell in each direction. The cell provides a convenient reference sampling of the macroscopic gas properties, while the collision partners are selected from the same subcell for the establishment of the collision rate. The dimensions of the cells must be such that the change in flow properties across each cell is small. The linear dimensions of the cells should be small in comparison with the scale length of the macroscopic flow gradients normal to streamwise directions, which means that the cell dimensions should be of the order of the local mean free path or even smaller^{23,24}.

The computational domain used for the calculation is made large enough so that body disturbances do not reach the upstream and side boundaries, where freestream conditions are specified. A schematic view of the computational domain is depicted in Fig. 2. Side I is defined by the body surface. Diffuse reflection with complete thermal accommodation is the condition applied to this side. Advantage of the flow symmetry is taken into account, and molecular simulation is applied to one-half of a full configuration. Thus, side II is a plane of symmetry. In such a boundary, all flow gradients normal to the plane are zero. At the molecular level, this plane is equivalent to a specular reflecting boundary. Side III is the freestream side through which simulated molecules enter and exit. Finally, the flow at the downstream outflow boundary, side IV, is predominantly supersonic and vacuum condition is specified¹⁷. At this boundary, simulated molecules can only exit.

Numerical accuracy in DSMC method depends on the grid resolution chosen as well as the number of particles per computational cell. Both effects were investigated to determine the number of cells and the number of particles required to achieve grid independence solutions for the thermal non-equilibrium flow that arises near the nose of the leading edges. Grid independence was tested by running the calculations with half and double the number of cells in each direction compared to a standard grid. Solutions were near identical for all grids used and were considered fully grid independent. A discussion of both effects on the aerodynamic surface quantities for power law shapes with zero-thickness nose ($t/\lambda_\infty = 0$) is described in details in Santos and Lewis⁸. The same procedure was adopted for the $t/\lambda_\infty > 0$ cases. However, the discussion will not be presented here.

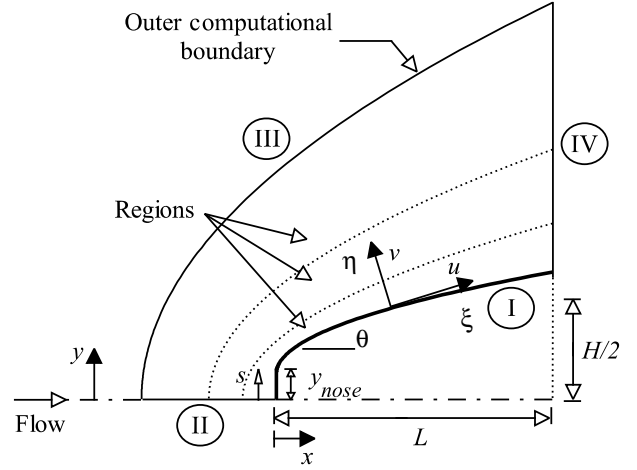


Figure 2. Schematic view of the computational domain.

V. Flow Conditions

The freestream flow conditions used for the numerical simulation of flow past the leading edges are those given by Santos and Lewis⁴ and summarized in Table 1, and the gas properties¹⁷ are shown in Table 2.

The freestream velocity V_∞ is assumed to be constant at 3.5 km/s, which corresponds to a freestream Mach number M_∞ of 12. The translational and vibrational temperatures in the freestream are in equilibrium at 220 K, and the leading edge surface has a constant wall temperature T_w of 880 K for all cases considered. The freestream Reynolds number by unit meter Re_∞ is 21455 based on conditions in the undisturbed stream.

The overall Knudsen number Kn_t , defined as λ_∞/t , corresponds to ∞ , 100, 10 and 1 for thickness, t/λ_∞ of 0, 0.01, 0.1 and 1, respectively. It is important to mention that $Kn_t = \infty$ case corresponds to the power law leading edge set already investigated by Santos and Lewis⁴.

Table 1. Freestream flow conditions

Altitude (km)	T_∞ (K)	p_∞ (N/m ²)	ρ_∞ (kg/m ³)	μ_∞ (Ns/m ²)	n_∞ (m ⁻³)	λ_∞ (m)
70	220.0	5.582	8.753×10^{-2}	1.455×10^{-2}	1.8209×10^{21}	9.03×10^{-4}

Table 2. Gas properties

X	m (kg)	d (m)	ω
O_2	5.312×10^{-26}	4.01×10^{-10}	0.77
N_2	4.650×10^{-26}	4.11×10^{-10}	0.74

VI. Computational Results and Discussions

Attention is now focused on the calculations of the aerodynamic surface quantities obtained from the DSMC results. Aerodynamic surface quantities of particular interest are number flux, heat transfer, pressure, skin friction and drag. Therefore, the purpose of this section is to discuss differences in these properties due to variations on the nose thickness of the power law bodies and to compare them to those obtained for the reference circular cylinder that generated the power law shapes. Comparisons based on geometry are made to examine the benefits and disadvantages of using these blunt geometries over circular cylinders.

A. Number Flux

The number flux N is calculated by sampling the molecules impinging on the surface by unit time and unit area. Results are normalized by $n_\infty V_\infty$, where n_∞ is the freestream number density and V_∞ is the freestream velocity.

The dependence of the dimensionless number flux to variations on the leading edge nose thickness is depicted in Figs. 3a to 3d for power law exponents of 2/3, 0.7, 3/4 and 0.8, respectively, as a function of the dimensionless arc length s/λ_∞ . Also, the dimensionless number flux for the circular cylinder case and that predicted by assuming free molecular (FM) flow¹⁷ are included for reference in this set of plots. It is seen from these figures that the dimensionless number flux to the front surface relies on the nose thickness in that it increases with increasing the thickness t . One possible reason for this behavior may be related to the collisions of two groups of molecules; the molecules reflecting from the nose of the leading edge and the molecules oncoming from the freestream. The molecules that are reflected from the body surface, which have a lower kinetic energy interact with the oncoming freestream molecules, which have a higher kinetic energy. Thus, the surface-reflected molecules re-collide with the body surface, which produce an increase in the dimensionless number flux in this region.

For a fixed power law exponent, it is also observed from these figures that the dimensionless number flux is high near the stagnation point and slightly decreases along the front surface up to the flat-face/afterbody junction with increasing the nose thickness (decreasing Kn_t). After that, it drops off sharply along the body surface. As the nose thickness decreases (increasing Kn_t), the dimensionless number flux approaches that limit value found for the zero-thickness case⁴ ($Kn_t = \infty$). As the power law exponent increases from 2/3 to 0.8, a reduction in the dimensionless number flux is observed for the nose thickness cases investigated. In addition, for the $Kn_t = 100$ case ($t/\lambda_\infty = 0.01$), the dimensionless number flux approaches the value ($N/n_\infty V_\infty = 1$) predicted by the free molecular flow equations¹⁷.

In general, the qualitative trend for the dimensionless number flux is as expected, approaching the limit value obtained by the free molecular flow equations as the nose thickness decreases and the power law exponent increases, i.e., as the leading edge becomes sharp, and approaching the circular cylinder behavior with increasing the nose thickness, i.e., as the leading edge becomes blunt.

B. Heat Transfer Coefficient

The heat flux q_w to the body surface is calculated by the net energy flux of the molecules impinging on the surface. The net heat flux q_w is related to the sum of the translational, rotational and vibrational energies of both incident and reflected molecules. A flux is regarded as positive if it is directed toward the body surface. The heat flux is normalized by $\rho_\infty V_\infty^3/2$ and presented in terms of heat transfer coefficient C_h .

The heat flux q_w to the body surface was defined in terms of the incident and reflected flow properties, and based upon the gas-surface interaction model of fully accommodated, complete diffuse re-emission. The diffuse model assumes that the molecules are reflected equally in all directions, quite independently of their incident speed and direction. Due to the diffuse reflection model, the reflected thermal velocity of the molecules impinging on the surface is obtained from a Maxwellian distribution that takes into account for the temperature of the body surface. In this fashion, as the wall temperature is the same for all the cases

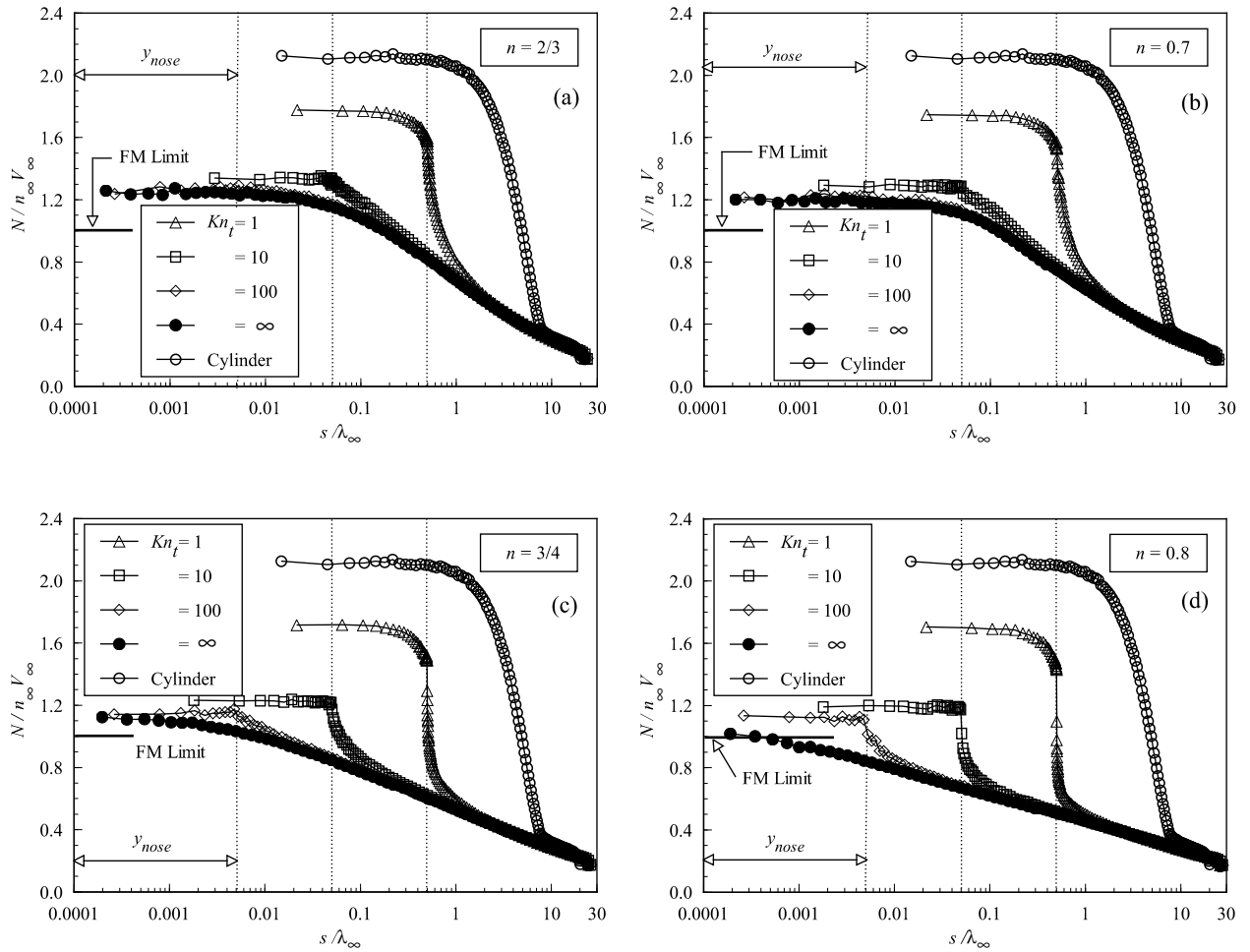


Figure 3. Dimensionless number flux $N/n_\infty V_\infty$ along the body surface as a function of the Knudsen number Kn_t for power-law afterbody exponents of (a) 2/3, (b) 0.6, (c) 3/4 and (d) 0.8.

investigated, the number of molecules impinging on the surface plays the important role on the reflected contribution to the net heat flux to the body surface.

The leading edge nose thickness effect on heat transfer coefficient C_h is plotted in Figs. 4a to 4d for power law exponents of 2/3, 0.7, 3/4 and 0.8, respectively, as a function of the dimensionless distance s/λ_∞ along the surface measured from the stagnation point. For comparison purpose, the heat transfer coefficient C_h for the circular cylinder case is also shown as well as that predicted by free molecular flow. It is seen from these figures that the heat transfer coefficient C_h is sensitive to the nose thickness. As would be expected, the flatter the leading edge is the lower the heat transfer coefficient at the stagnation point. Also, the heat transfer coefficient remains essentially constant over the first half of the front surface, but then increases in the vicinity of the flat-face/afterbody junction for the flattest case investigated, $Kn_t = 1$ ($t/\lambda_\infty = 1$). Subsequently, the heat transfer coefficient decreases sharply and continues to decline along the body surface.

Usually, the stagnation region is generally considered as being the most thermally stressed zone in sharp/blunt bodies, as shown by the power law cases investigated defined by $Kn_t = \infty$ ($t/\lambda_\infty = 0$). Nevertheless, as a flat nose is introduced in these power law shapes, the most severe heat transfer region moves to

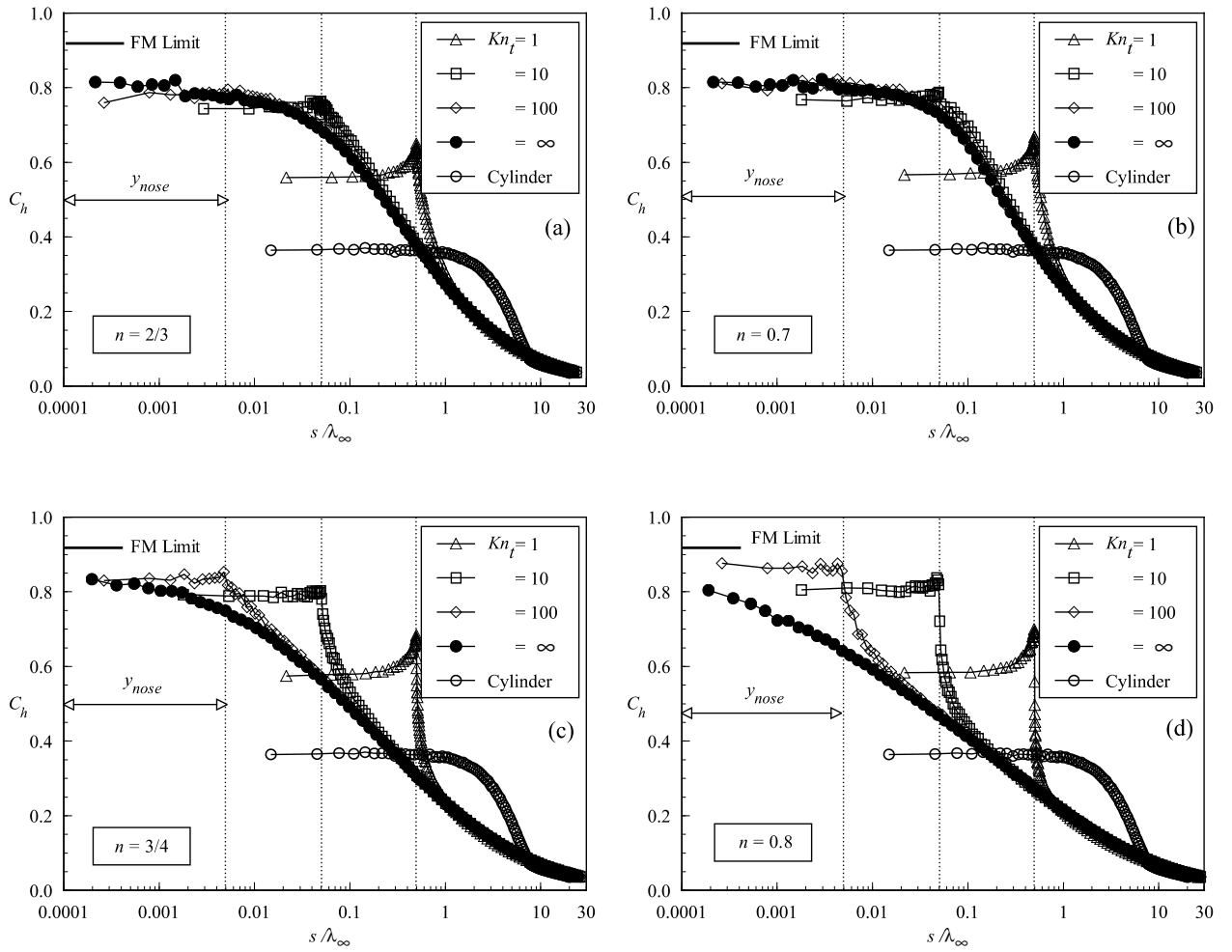


Figure 4. Heat transfer coefficient C_h along the body surface as a function of the Knudsen number Kn_t for power-law afterbody exponents of (a) 2/3, (b) 0.6, (c) 3/4 and (d) 0.8.

the flat-face/afterbody junction. As the number of molecules impinging on the front surface decreases in the vicinity of the flat-face/afterbody junction (see Fig. 3), then the velocity of the molecules increases as the flow approaches the junction of the leading edge in order to increase the heat transfer coefficient. Moreover, the contribution of the translational energy to the net heat flux varies with the square of the thermal velocity of the molecules.

The heat transfer coefficient at the stagnation point predicted by the free molecular equations¹⁷ is $C_{ho} = 0.912$, as shown in Figs. 4a to 4d. According to these figures, the stagnation point heating tends to this limit value as the leading edge becomes sharp, i.e., by reducing the nose thickness of the leading edges (increasing Kn_t) and by increasing the power law exponent n .

In contrast to the power law bodies, the heat transfer coefficient C_h for the circular cylinder remains essentially constant over the first half of the cylindrically portion of the leading edge, but then decreases sharply up to the cylinder/wedge junction. In addition, the heat transfer coefficient over the circular cylinder varies by an order of magnitude from the stagnation point to the cylinder/wedge junction. By considering that the heat transfer coefficient at the stagnation point C_{ho} as well as C_h is inversely proportional to \sqrt{R} for

the circular cylinder case, then decreasing the nose radius increases the value of dC_h/ds by the factor $1/R^{3/2}$. Consequently, for small nose radius dC_h/ds is very large and, therefore, conduction plays an important role.

At this point, it seems important to compare the heat transfer coefficient at the stagnation point of the flat-nose power-law shapes $(C_{ho})_{pwr}$ with that for the circular cylinder $(C_{ho})_{cyl}$ that generated the power law shapes. Table 3 displays the ratio of $(C_{ho})_{pwr}$ to $(C_{ho})_{cyl} = 0.366$ for the cases investigated as a function of the Knudsen number Kn_t . According to Table 3, a substantial reduction in the heat transfer coefficient at the stagnation point is obtained by introducing the flat nose in the power law shapes. As a reference, for power law exponent of 2/3, $(C_{ho})_{pwr}$ reduces from 114.5% to 52.7%, compared to $(C_{ho})_{cyl}$, when the dimensionless nose thickness t/λ_∞ increases from 0 to 1. It is also noted that a similar behavior is obtained to power law exponent of 0.8, changing from 140.2% to 59.6% for the same variation in the nose thickness.

Table 3. Heat transfer coefficient comparison at the stagnation point, $(C_{ho})_{pwr}/(C_{ho})_{cyl}$.

Exp. n	$Kn_t = \infty$	$Kn_t = 100$	$Kn_t = 10$	$Kn_t = 1$
2/3	2.145	2.123	2.033	1.527
0.6	2.243	2.235	2.098	1.549
3/4	2.344	2.273	2.156	1.574
0.8	2.402	2.374	2.205	1.596

Referring to Table 3, it is also observed a considerable reduction in the heat transfer coefficients of the new power law shapes when they are compared to the corresponding zero-thickness cases. For the zero-thickness cases ($Kn_t = \infty$), the heat transfer coefficient increased by around 12% as the power law exponent increased from 2/3 to 0.8. In contrast, for the $t/\lambda_\infty = 1$ case ($Kn_t = 1$), the heat transfer coefficient increased only 4.5% as the power law exponent increased from 2/3 to 0.8.

C. Pressure Coefficient

The pressure p_w on the body surface is calculated by the sum of the normal momentum fluxes of both incident and reflected molecules at each time step. Results are presented in terms of the pressure coefficient C_p .

The variation of the pressure coefficient C_p caused by changes in the leading edge nose thickness is demonstrated in Figs. 5a to 5d for power law exponents of 2/3, 0.7, 3/4 and 0.8, respectively. It can be noted from these figures that the pressure coefficient is high along the front surface, basically a constant value along it, and decreases dramatically along the afterbody surface in the vicinity of the flat-face/afterbody junction. This effect is more pronounced with decreasing Knudsen number Kn_t , i.e., as the nose becomes flatter.

Plotted along with the computational solution for pressure coefficient is the pressure coefficient predicted by the free molecular flow equations and that for the circular cylinder. For the circular cylinder case, the pressure coefficient C_p follows the same trend presented by the heat transfer coefficient in that it remains constant over the first half of the cylindrical portion of the leading edge, but then decreases sharply up to the cylinder/wedge junction. Also, the pressure coefficient C_p varies by one order of magnitude from the stagnation point to the cylinder/wedge junction.

The pressure coefficient C_p predicted by the free molecular flow equations on the front surface is 2.35. Therefore, for the thinnest flat leading edge investigated, $t/\lambda_\infty = 0.01$, which corresponds to $Kn_t = 100$, the flow seems to approach the free collision flow in the vicinity of the stagnation point (Fig. 5d), as was pointed out earlier.

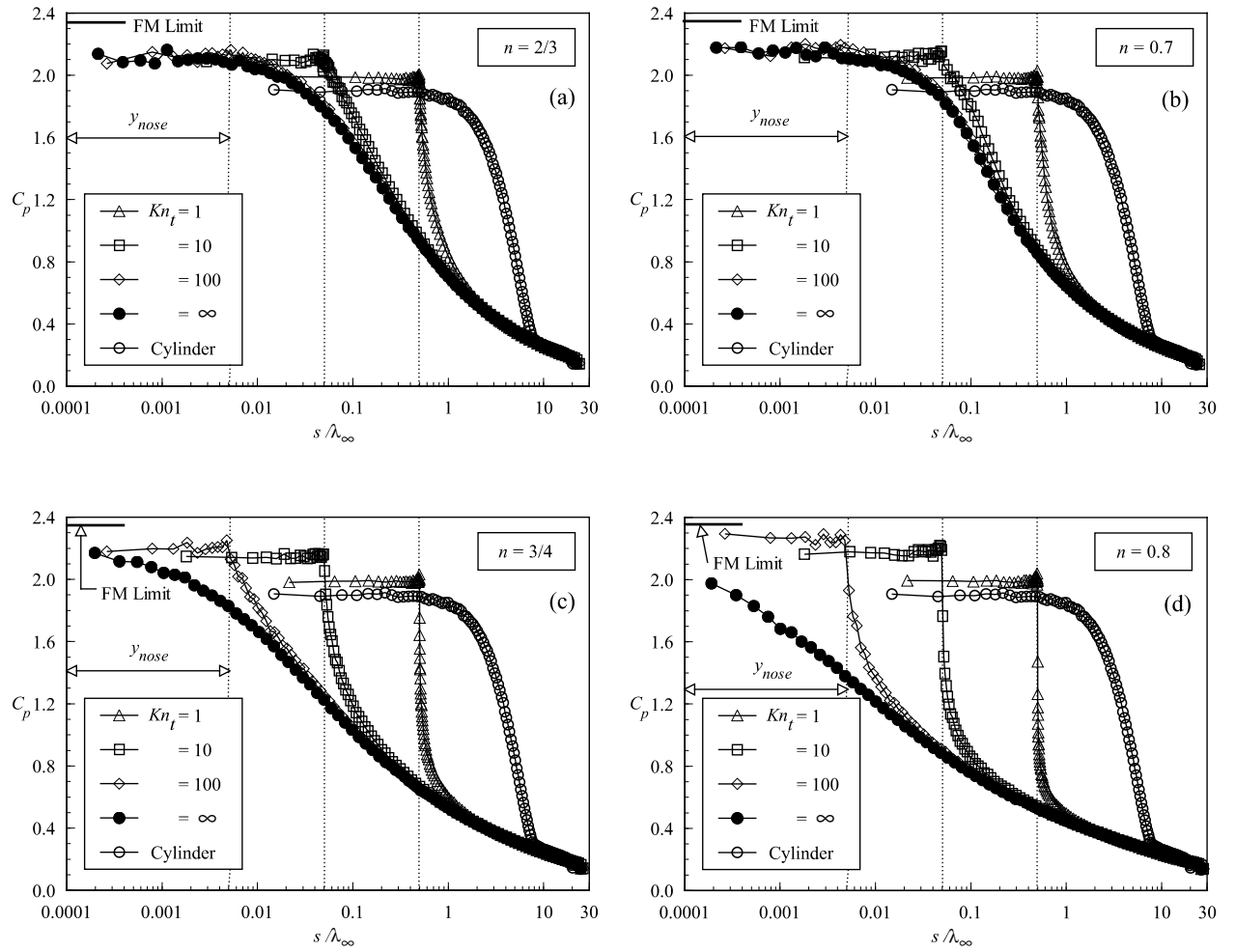


Figure 5. Pressure coefficient C_p along the body surface as a function of the Knudsen number Kn_t for power-law afterbody exponents of (a) 2/3, (b) 0.6, (c) 3/4 and (d) 0.8.

D. Skin Friction Coefficient

The shear stress τ_w on the body surface is calculated by averaging the tangential momentum transfer of the molecules impinging on the surface. For the diffuse reflection model imposed for the gas-surface interaction, reflected molecules have a tangential moment equal to zero, since the molecules essentially lose, on average, their tangential velocity component.

The shear stress τ_w on the body surface is normalized by $\rho_\infty V_\infty^2/2$ and presented in terms of the dimensionless skin friction coefficient C_f . The influence of the leading edge nose thickness on the skin friction coefficient obtained by DSMC method is displayed in Figs. 6a to 6d for power law exponents of 2/3, 0.7, 3/4 and 0.8, respectively, and parameterized by the thickness Knudsen number. According to these figures, the skin friction coefficient C_f is zero at the stagnation point and slightly increases along the front surface up to the flat-face/afterbody junction of the leading edge. After that, C_f increases meaningfully to a maximum value that depends on the nose thickness, and decreases downstream along the body surface by approaching the skin friction coefficient predicted by the reference case of zero thickness, $Kn_t = \infty$. In addition, smaller

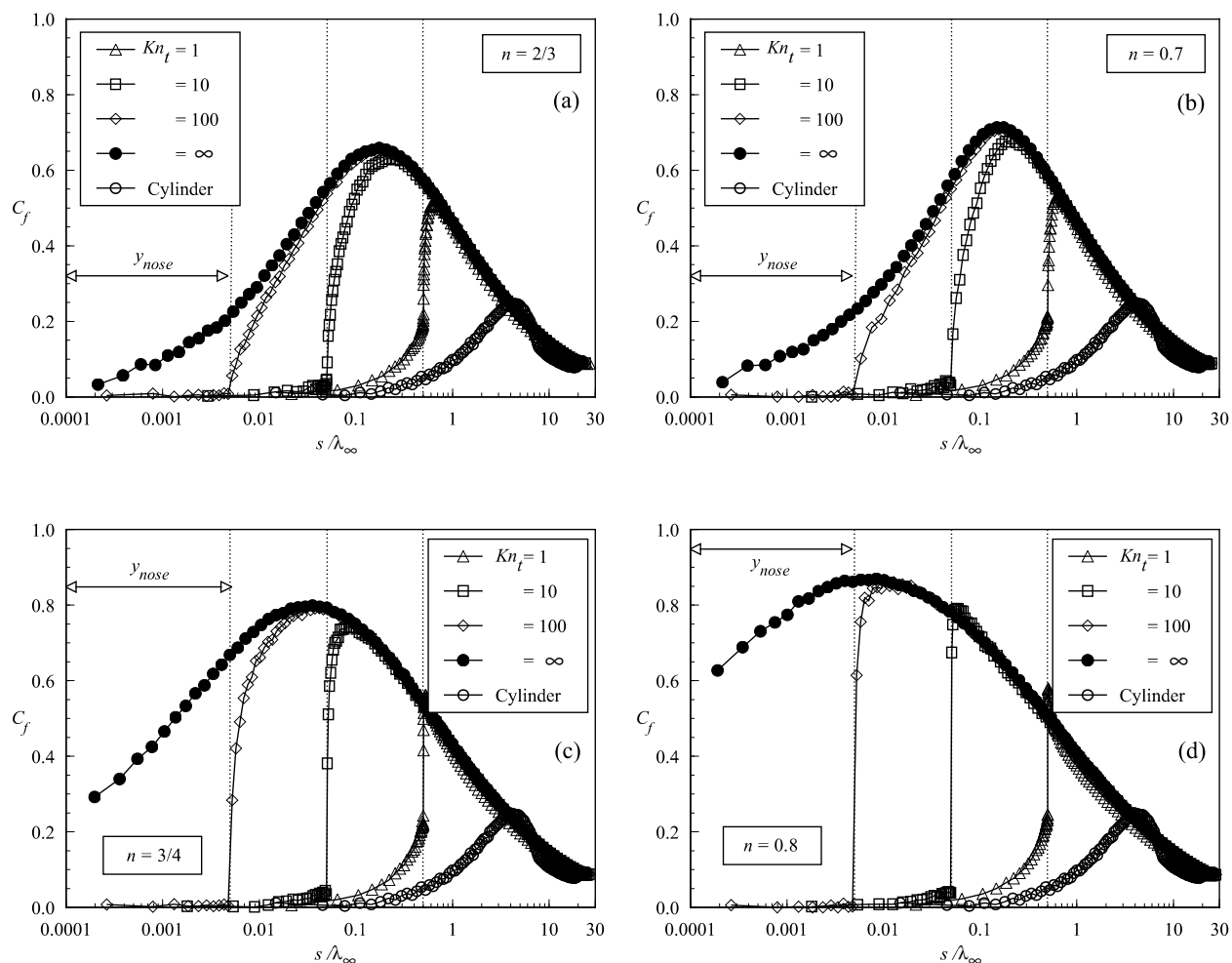


Figure 6. Skin friction coefficient C_f along the body surface as a function of the Knudsen number Kn_t for power-law afterbody exponents of (a) 2/3, (b) 0.6, (c) 3/4 and (d) 0.8.

thickness t (larger Kn_t) leads to higher peak value for the skin friction coefficient C_f . Also, smaller thickness t displaces the peak value to near the flat-face/afterbody junction.

The skin friction coefficient C_f predicted by the free molecular flow equations¹⁷ is zero along the frontal surface of the bodies and exhibits its maximum value on the afterbody surface at a station that corresponds to a body slope of 45 degree (not shown). Similarly, the maximum values of C_f for the nose thicknesses investigated occur very close to the same station. The number of molecules by unit time and unit area impinging on the body is high on the front surface of the leading edge and low on the afterbody portion of the body (see Fig. 3). In contrast, the tangential component of the molecular velocity is basically zero on the front surface and high along the afterbody surface (due to the flow expansion), where the velocities of the molecules are those that are more characteristic of the freestream velocity. As a result, the product of both properties, which is proportional to the shear stress (skin friction coefficient), presents the maximum value around station of 45 degree. Furthermore, attention should be paid to the fact that a body slope of 45 degree corresponds to a different arc length s/λ_∞ for the nose thicknesses investigated. Also, as the power

law exponent n increases the arc length s/λ_∞ corresponding to a slope of 45 degree approaches the shoulder of the shapes.

E. Total Drag Coefficient

The drag on a surface in a gas flow results from the interchange of momentum between the surface and the molecules colliding with the surface. The total drag is obtained by the integration of the pressure p_w and shear stress τ_w distributions from the stagnation point of the leading edge to the station L that corresponds to the tangent point common to all the leading edges (see Fig. 1). It is important to mention that the values for the total drag were obtained by assuming the shapes acting as leading edges. Therefore, no base pressure effects were taken into account on the calculations. Results for total drag are normalized by $\rho_\infty V_\infty^2 H/2$ and presented as total drag coefficient C_d and its components of pressure drag coefficient C_{pd} and the skin friction drag coefficient C_{fd} .

The extent of the changes in the total drag coefficient C_d with the leading edge nose thickness is demonstrated in Fig. 7a to 7d for power law exponents of 2/3, 0.7, 3/4 and 0.8, respectively, along with the drag coefficient for the circular cylinder case. It is seen that as the leading edge becomes flatter the contribution of the pressure drag C_{pd} to the total drag increases and the contribution of the skin friction drag C_{fd} decreases. As the net effect on total drag coefficient C_d depends on these two opposite behaviors, hence no appreciable changes are observed in the total drag coefficient for the nose thicknesses investigated.

Referring to Figs. 7a to 7d, it can be seen that the total drag coefficient C_d increased slightly by a rise in the nose thickness t . The major contribution to the total drag coefficient is attributed to the skin friction coefficient, which decreases with increasing the nose thickness t . In contrast, for the circular cylinder case, the major contribution to the total drag coefficient is attributed to the pressure, that accounts for 89% of the total drag.

At this point, it seems important to compare the total drag coefficient of the flat-nose power-law shapes $(C_d)_{pwr}$ with that for the circular cylinder $(C_d)_{cyl}$ that generated the power law shapes. Table 4 illustrates the ratio of $(C_d)_{pwr}$ to $(C_d)_{cyl} = 1.519$ for the cases investigated as a function of the Knudsen number Kn_t . According to Table 4, appreciable changes are observed in the total drag coefficient by introducing the flat nose in the power law shapes. As a reference, for power law exponent of 2/3, $(C_d)_{pwr}$ increases from 71.0% to only 72.3%, compared to $(C_d)_{cyl}$, when the dimensionless nose thickness t/λ_∞ increases from 0 to 1. It is also noted that a similar behavior is obtained to power law exponent of 0.8, changing from 67.6% to 68.5% for the same variation in the nose thickness.

Table 4. Comparison of the total drag coefficient for flat-nose power-law shapes with that for the circular cylinder, $(C_d)_{pwr}/(C_d)_{cyl}$.

Exp. n	$Kn_t = \infty$	$Kn_t = 100$	$Kn_t = 10$	$Kn_t = 1$
2/3	0.710	0.711	0.711	0.723
0.6	0.716	0.716	0.716	0.724
3/4	0.687	0.688	0.688	0.697
0.8	0.676	0.677	0.677	0.685

VII. Concluding Remarks

The computations of a rarefied hypersonic flow on blunt bodies have been performed by using the Direct Simulation Monte Carlo method. The calculations provided information concerning the nature of the aerodynamic surface quantities for a family of contours composed by a flat nose followed by a curved afterbody

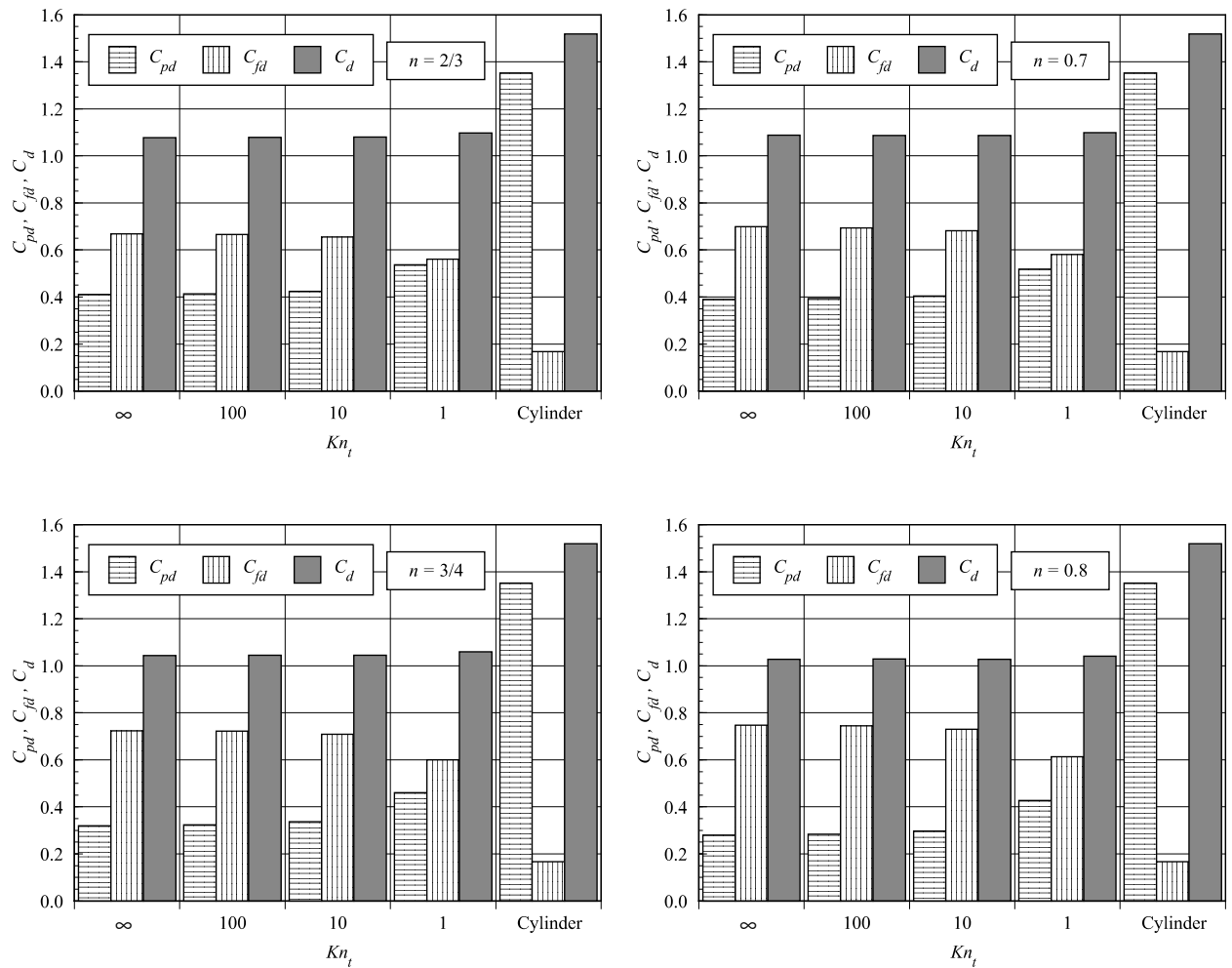


Figure 7. Pressure drag C_{pd} , skin friction drag C_{fd} and total drag C_d coefficients as a function of the Knudsen number Kn_t for power-law afterbody exponents of (a) 2/3, (b) 0.6, (c) 3/4 and (d) 0.8.

surface defined by power-law shapes.

The aerodynamic performance of these blunt shapes was compared to a corresponding circular cylinder leading edge shape, typically used in blunting sharp leading edges for heat transfer considerations. It was found that the stagnation point heating is still higher and the total drag is lower on the new blunt shapes than the representative circular cylinder solution in this geometric comparison. Thus, in general, these shapes behave as if they had a sharper profile than their representative circular cylinder. However, these shapes have more volume than the circular cylinder geometry. Hence, although stagnation point heating on these new shapes may be higher as compared to the circular cylinder, the overall heat transfer to these leading edges may be tolerate if there is an active cooling because additional coolant may be placed in the leading edge. Moreover, shock standoff distance on a cylinder scales with the radius of curvature, therefore cylindrical bluntness added for heating rate reduction will also tend to displace the shock wave, allowing pressure leakage. In this context, as the new shapes behave as if they were sharper profiles than the circular cylinder, they may display smaller shock detachment distances than the corresponding circular cylinder. Nevertheless, the shock wave structure on these new shapes is the subject for future work.

Acknowledgments

The financial support provided by Fundação de Amparo à Pesquisa do Estado de São Paulo (grant FAPESP 2003/01765-9) is gratefully acknowledged.

References

- ¹Mason, W. H. and Lee, J., “Aerodynamically Blunt and Sharp Bodies,” *Journal of Spacecraft and Rockets*, Vol. 31, No. 3, 1994, pp. 378–382.
- ²O’Brien, T. F. and Lewis, M. J., “Power Law Shapes for Leading-Edge Blunting with Minimal Shock Standoff,” *Journal of Spacecraft and Rockets*, Vol. 36, No. 5, 1999, pp. 653–658.
- ³Santos, W. F. N., “Direct Simulation Monte Carlo of Rarefied Hypersonic Flow on Power Law Shaped Leading Edges,” Ph.D. Dissertation, Dept. of Aerospace Engineering, University of Maryland, College Park, MD, Dec., 2001.
- ⁴Santos, W. F. N., and Lewis, M. J., “Power Law Shaped Leading Edges in Rarefied Hypersonic Flow,” *Journal of Spacecraft and Rockets*, Vol. 39, No. 6, 2002, pp. 917–925.
- ⁵Santos, W. F. N., and Lewis, M. J., “Angle of Attack Effect on Rarefied Hypersonic Flow over Power Law Shaped Leading Edges,” in *23rd International Symposium on Rarefied Gas Dynamics*, Whistler, BC, Canada, July 20-25, 2002.
- ⁶Santos, W. F. N., and Lewis, M. J., “Shock Wave Structure in a Rarefied Hypersonic Flow on Power Law Shaped Leading Edges,” in *41st AIAA Aerospace Sciences Meeting and Exhibit*, AIAA Paper 2003-1134, Reno, NV, January 6-9, 2003.
- ⁷Santos, W. F. N., and Lewis, M. J., “Aerodynamic Heating Performance of Power Law Leading Edges in Rarefied Hypersonic Flow,” in *36th AIAA Thermophysics Conference*, AIAA Paper 2003-3894, Orlando, FL, June 23-26, 2003.
- ⁸Santos, W. F. N., and Lewis, M. J., “Effects of Compressibility on Rarefied Hypersonic Flow over Power Law Leading Edges,” in *42nd AIAA Aerospace Sciences Meeting and Exhibit*, AIAA Paper 2004-1181, Reno, NV, January 5-8, 2004.
- ⁹Santos, W. F. N., and Lewis, M. J., “Calculation of Shock Wave Structure over Power Law Bodies in Hypersonic Flow,” *Journal of Spacecraft and Rockets*, To appear, in press.
- ¹⁰Nonweiler, T. R. F., “Aerodynamic Problems of Manned Space Vehicles,” *Journal of the Royal Aeronautical Society*, Vol. 63, Sept, 1959, pp. 521–528.
- ¹¹Anderson, J. L., “Tethered Aerothermodynamic Research for Hypersonic Waveriders,” in *Proceedings of the 1st International Hypersonic Waverider Symposium*, Univ. of Maryland, College Park, MD, 1990.
- ¹²Potter, J. L. and Rockaway, J. K., “Aerodynamic Optimization for Hypersonic Flight at Very High Altitudes,” in *Rarefied gas Dynamics: Space Science and Engineering*, edited by B. D. Shizgal and D. P. Weaver, Vol. 160, Progress in Astronautics and Aeronautics, AIAA New York, 1994, pp.296-307.
- ¹³Rault, D. F. G., “Aerodynamic Characteristics of a Hypersonic Viscous Optimized Waverider at High Altitude,” *Journal of Spacecraft and Rockets*, Vol. 31, No. 5, 1994, pp. 719–727.
- ¹⁴Graves, R. E. and Argrow, B. M., “Aerodynamic Performance of an Osculating-Cones Waverider at High Altitudes,” in *35th AIAA Thermophysics Conference*, AIAA Paper 2001-2960, Anaheim, CA, 2001.
- ¹⁵Reller Jr., J. O., 1957, “Heat Transfer to Blunt Nose Shapes with Laminar Boundary Layers at High Supersonic Speeds,” NACA RM-A57FO3a, 1957.
- ¹⁶Schaaf, S. A. and Chambre, P. L., *Flow of Rarefied Gases*, Princeton Aeronautical Paperbacks, Princeton University Press, Princeton, NJ, 1961.
- ¹⁷Bird, G. A., *Molecular Gas Dynamics and the Direct Simulation of Gas Flows*, Oxford University Press, Oxford, England, UK, 1994.
- ¹⁸Bird, G. A., “Monte Carlo Simulation in an Engineering Context,” in *Progress in Astronautics and Aeronautics: Rarefied gas Dynamics*, edited by Sam S. Fisher, Vol. 74, part I, AIAA New York, 1981, pp. 239–255.
- ¹⁹Bird, G. A., “Perception of Numerical Method in Rarefied Gasdynamics, in *Rarefied gas Dynamics: Theoretical and Computational Techniques*,” edited by E. P. Muntz, and D. P. Weaver and D. H. Capbell, Vol. 118, Progress in Astronautics and Aeronautics, AIAA, New York, 1989, pp. 374–395.
- ²⁰Garcia, A. L., and, Wagner, W., “Time Step Truncation Error in Direct Simulation Monte Carlo,” *Physics of Fluids*, Vol. 12, No. 10, 2000, pp. 2621–2633.
- ²¹Hadjiconstantinou, N. G., “Analysis of Discretization in the Direct Simulation Monte Carlo,” *Physics of Fluids*, Vol. 12, No. 10, 2000, pp. 2634–2638.
- ²²Borgnakke, C. and Larsen, P. S., “Statistical Collision Model for Monte Carlo Simulation of Polyatomic Gas Mixture,” *Journal of computational Physics*, Vol. 18, No. 4, 1975, pp. 405–420.
- ²³Alexander, F. J., Garcia, A. L., and, Alder, B. J., “Cell Size Dependence of Transport Coefficient in Stochastic Particle Algorithms,” *Physics of Fluids*, Vol. 10, No. 6, 1998, pp. 1540–1542.
- ²⁴Alexander, F. J., Garcia, A. L., and, Alder, B. J., “Erratum: Cell Size Dependence of Transport Coefficient is Stochastic Particle Algorithms,” *Physics of Fluids*, Vol. 12, No. 3, 2000, pp. 731–731.